

Mixed Proton and Oxide Ion Conduction, Phase Stability, and Conducting Mechanisms in the Sr_2CeO_4 -based Materials

Wenzhuo Chen¹, Jungu Xu^{1,*}, Chenjie Lou², Mingxue Tang^{2,3*}, Xia Deng¹, Jiasheng Lv¹, Jing Fang¹, Jibran Khaliq⁴, Laijun Liu^{1,*}, Qi Zhang^{5,6*}

1. *Guangxi Universities Key Laboratory of Non-ferrous Metal Oxide Electronic Functional Materials and Devices, MOE Key Laboratory of New Processing Technology for Nonferrous Metals and Materials, College of Materials Science and Engineering, Collaborative Innovation Center for Exploration of Nonferrous Metal Deposits and Efficient Utilization of Resources, Guilin University of Technology, Guilin, Guangxi, 541004, China.*
2. *Center for High Pressure Science and Technology Advanced Research, Beijing 100193, China.*
3. *College of Materials Science and Engineering, University of Science and Technology Beijing, Beijing 100083, China*
4. *Department of Mechanical and Construction Engineering, Faculty of Engineering and Environment, Northumbria University, Newcastle, Newcastle upon Tyne, UK*
5. *BCMaterials, Basque Centre for Materials, Applications and Nanostructures, UPV/EHU Science Park, 48940 Leioa, Spain*
6. *IKERBASQUE, Basque Foundation for Science, Plaza Euskadi, 5, 48009 Bilbao, Spain*

* Corresponding Author: xujungu@glut.edu.cn; mxtang@ustb.edu.cn; ljliu2@163.com; qi.zhang@bcmaterials.net;

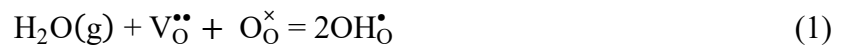
Abstract

Sr_2CeO_4 possesses structural characteristic of one-dimensional (1D) edge-sharing CeO_6 octahedral chains, exhibits superior phase and chemical stability compared to the perovskite SrCeO_3 . There have been previous attempts to improve electrical conductivity through proton conduction by acceptor-doping of Yb on the Ce site. However, its electrical conductivity remained low, for instance, at 500 °C, the reported value was 3.16×10^{-7} S/cm, hence limiting its practical applications. In this paper, we synthesized four new rare earth doped $\text{Sr}_2\text{Ce}_{0.95}\text{M}_{0.05}\text{O}_{3.975}$ (where M = Y, Dy, Er, Tb) by the solid state reaction method. We thoroughly investigated their phases, electrical properties, and stability. Additionally, for the first time, we investigated the proton and oxide ion conduction mechanisms in Sr_2CeO_4 -based materials using a bond-valence-based method. This analysis revealed a clear 1D conduction along the *c*-axis within the CeO_6 tetrahedral chains and 2D conduction within the *a-c* plane, respectively. The findings revealed that all doped materials showed obvious proton conduction, alongside partial oxide ion conduction. Notably, the Er-, Dy-, and Y-doped samples demonstrated significantly improved conductivity under wet condition (with a water partial pressure of ~ 0.03 atm) at 500 °C, reaching approximately $\sim 10^{-4}$ S/cm. This is nearly three orders of magnitude higher than the previously reported Yb-doped Sr_2CeO_4 .

Keywords: Sr_2CeO_4 , Mixed Ion Conduction, Rare-earth Doped, Phase Instability, Ion Migration Pathway Simulation

Introduction

Solid oxide fuel cells (SOFCs) are attracting more and more attention due to their promising pollution-free and high energy conversion efficiency advantages [1-5]. Depending on the type of charge carrier in the electrolyte, SOFCs could be divided into oxide ion conducting fuel cells (O-SOFCs) and proton conducting fuel cells (PC-SOFC). The commonly utilized oxide ion electrolyte material for SOFCs is yttrium (or yttria)-stabilized ZrO_2 (YSZ); however, it only reaches satisfactory conductivity level at temperature higher than 800 °C [6, 7]. Such a high operating temperature would cause the degradation of the materials and the compatibility issues between the electrodes and electrolyte. In addition, although oxide ion conductor based SOFCs materials have good tolerance to fuel types (methane, coal gas, hydrogen), the water or carbon dioxide formed on the fuel side (anode) will dilute the fuel, thereby reducing fuel efficiency. Therefore, water management at the electrodes and reducing operating temperature will be the main challenges for the O-SOFC. By comparison, protons pass through the electrolyte from the anode to the cathode and form water on the cathode side. This will not only avoid diluting the fuel, but also reduce the risk of anode oxidation and increase the service life of the electrolyte material. Moreover, proton conductors have lower proton transporting barriers and relatively higher ionic conductivity compared to oxide ion conductors, which usually allows relatively lower operating temperature (about 400-800 °C) [8-12]. For proton conduction, the presence of oxygen vacancies is crucial for the formation of protons, as can be described according to Eq. (1)



where $\text{V}_{\text{O}}^{\bullet\bullet}$ is the oxygen vacancy, $\text{O}_{\text{O}}^{\times}$ denotes the position of regular oxygen atom, and $\text{OH}_{\text{O}}^{\bullet}$ is the hydroxy group in the oxygen sublattice [13]. Currently, the most extensively studied proton

conductors are acceptor-doped perovskite materials based on SrCeO_3 or BaCeO_3 . These materials exhibit proton conductivities typically within the temperature range of 400-800 °C. However, the chemical stability of these materials under CO_2 and H_2O atmospheres is relatively low. This is crucial for their utilization as electrolytes in hydrocarbon- or syngas-fueled SOFCs, limiting its practical applications [14-17]. Conversely, Sr_2CeO_4 , another compound in the CeO_2 - SrO system, features a non-perovskite structure with an orthorhombic crystal structure containing intriguing 1D chains of edge-sharing CeO_6 octahedra along the c -axis, as displayed in **Figure 1**. This material has demonstrated significantly improved physical and chemical stabilities compared to the perovskite SrCeO_3 [18-20]. Building upon this, Gorelov et al investigated the electrical transport properties of acceptor-doped $\text{Sr}_2\text{Ce}_{0.95}\text{Yb}_{0.05}\text{O}_{4-\alpha}$ [20]. Their findings revealed that while high-temperature ionic conductivity was primarily oxide ion conduction, at lower temperature (400-500 °C), the proton conduction dominated. However, both oxide ion conduction (measuring 5.62×10^{-5} S/cm at 800 °C) and proton conduction (measuring 3.16×10^{-7} S/cm at 500 °C) were insufficient to meet the requirements for practical application.

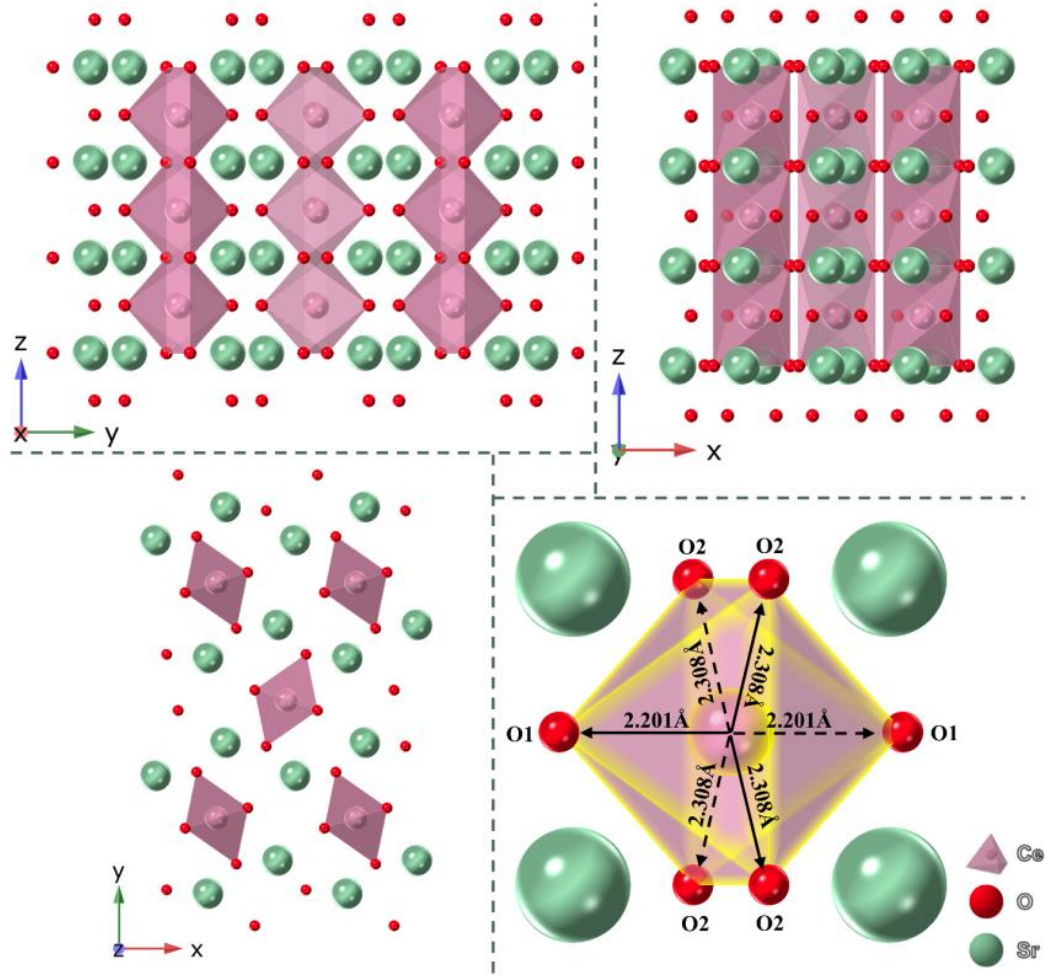


Figure 1. Crystal structure of Sr_2CeO_4 .

In this study, to further explore the potential of Sr_2CeO_4 as an electrolyte for SOFCs, four novel rare earth-doped materials, $\text{Sr}_2\text{Ce}_{0.05}\text{M}_{0.95}\text{O}_{3.975}$ (where $\text{M} = \text{Y}, \text{Dy}, \text{Er}, \text{Tb}$) were synthesized using the solid state reaction method. In this paper, their phases, electrical properties, stabilities, and conducting mechanisms thoroughly examined and reported.

Experimental

Materials Synthesis and Preparation. A series of rare earth doped Sr_2CeO_4 ceramic samples were prepared using a traditional solid state reaction (SSR) method. Raw materials including SrCO_3 (99.95%, Aladdin), CeO_2 (99.95%, Aladdin), Er_2O_3 (99.90%, Aladdin), Dy_2O_3 (99.90%, Aladdin),

Tb₄O₇ (99.90%, Aladdin), and Y₂O₃ (99.90%, Aladdin) were used with prior heating treatment (These raw materials were all produced by Shanghai Aladdin Biochemical Technology Co., Ltd. in China). All raw materials except SrCO₃ were precalcined at 1000 °C for 3 h before weighing. Raw materials were weighed according to the stoichiometric ratio. The powders were ball-milled with ethanol for 6 h and the resulting slurries were placed in an oven at 60 °C for 12 h to remove ethanol. Calcination of the powders were carried out at 900 °C for 8 h and then reground to break the agglomerates. The resulting powder was cold pressed into disks (diameter ~15 mm. thickness ~10 mm). The samples were sintered at 1150 °C for 8 h in air and the sintered samples were ground to obtain flat surface for characterization.

Characterization. Panalytical X'Pert PRO (XRD, PANalytical, Almelo, Netherlands) diffractometer (Cu-K α radiation) were used to obtain XRD spectra. The data were recorded over a 2θ range of 10° to 65°, with a step size of 0.02°. Electrochemical impedance spectroscopy (EIS) measurements were performed with a Bio-Logic VSP (EIS, Bio-Logic, Grenoble, France) instrument over a 10⁶ to 10⁻¹ Hz frequency range. The Rietveld and Pawley refinements against these diffraction data were carried out with the Topas-Academic software [21]. Scanning electron microscope (SEM) and energy disperse spectrum (EDS) analysis was carried out on the GeminiSEM 300 (SEM-EDS, Carl Zeiss, Oberkoche, Germany) scanning electron microscope, with operating voltage of 15 kV. X-ray photoelectron spectroscopy (XPS) was recorded on ESCALAB 250Xi, Thermo Scientific (America), and a vacuum of 10⁻¹⁰ mbar was applied. Room temperature electron paramagnetic resonance (EPR) experiments were performed at on a CIQTEK EPR200-Plus spectrometer equipped with a high-sensitivity cavity in X-band, with frequency ~ 9.7 GHz and the microwave power of 0.2 mW. The spectra were calibrated by the sample weight, applied power and the Q factors. For the EIS

measurements, electrodes were fabricated by coating platinum paste on opposite sides of the pellets and then fired at 850 °C for 2 h in air. An equilibrium time of 30 mins for each temperature was set before the impedance measurements. The wet atmospheres used in this work for the electrical property measurements were achieved by simply bubbling a specific gas through the room temperature water and then fed into the tube furnace, with the water partial pressure ($P_{\text{H}_2\text{O}}$) of $\sim 3.13 \times 10^{-2}$ atm or other value that specified in the text. The distribution of relaxation times (DRT) analysis was performed using the EISART software developed by Li Hangyue et. al from Tsinghua university [22].

Results and Discussions

Phases and structures. Figure 2a shows the XRD patterns of both virgin and doped Sr_2CeO_4 materials. It is evident that all samples exhibited a single phase closely matching the orthorhombic Sr_2CeO_4 phase (PDF#50-0115), with lattice parameters of $a \approx 6.11897$ Å, $b \approx 10.34950$ Å, $c \approx 3.59700$ Å. Rietveld refinement showed a good fit for XRD data of all the samples using as shown in Figure 2b, indicating the successful substitutions of dopants in the virgin structure giving a single phase. Specific finishing parameters are shown in Table S1.

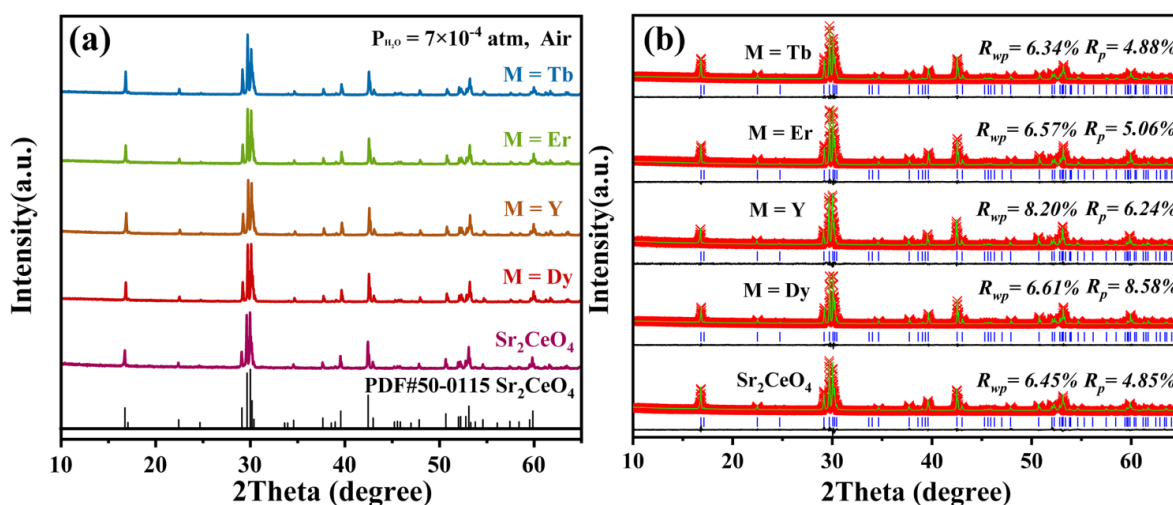


Figure 2. (a) XRD pattern of the $\text{Sr}_2\text{Ce}_{0.95}\text{M}_{0.05}\text{O}_{3.975}$ (M = Y, Dy, Er, Tb); (b) $\text{Sr}_2\text{Ce}_{0.95}\text{M}_{0.05}\text{O}_{3.975}$ (M

= Y, Dy, Er, Tb) Rietveld refinements plot.

Electrical properties. The AC impedance spectroscopy technique was used to investigate the electrical properties of $\text{Sr}_2\text{Ce}_{0.95}\text{M}_{0.05}\text{O}_{3.975}$. **Figure 3a** presents the electrical conductivities of both virgin and doped Sr_2CeO_4 materials over the temperature range of 300–750 °C under dry and wet N_2 ($P_{\text{H}_2\text{O}} \approx 0.03$ atm) environments. Electrical conductivity under wet atmosphere was significantly enhanced compared to dry conditions, particularly ≤ 500 °C. For instance, the Er-doped Sr_2CeO_4 exhibited an enhancement of more than three orders of magnitude, increasing from 1.38×10^{-7} S/cm under dry N_2 environment to 1.08×10^{-4} S/cm under wet N_2 . Even the virgin Sr_2CeO_4 showed conductivity level nearly one order of magnitude higher under wet N_2 compared to dry N_2 at temperature ≤ 500 °C, due to the intrinsic oxygen vacancies in the material. For the parent Sr_2CeO_4 sample, activation energy E_a under wet atmosphere is ~ 0.93 eV which is slightly higher than that 0.87 eV reported in Yadav et al's work [23]. However, no data for the conductivity of the parent Sr_2CeO_4 sample under wet atmosphere was reported in literature to be compared with the value of 0.97 eV in our work. For the doped samples, here taking the Er-doped $\text{Sr}_2\text{Ce}_{0.95}\text{Er}_{0.05}\text{O}_{3.975}$ sample for example, under dry atmospheres ($P_{\text{H}_2\text{O}} \sim 7 \times 10^{-4}$ atm), the calculated E_a in the temperature region ≤ 500 °C is about 0.94 eV, lower than that (1.22 eV) reported in Gorelov et al's work for the Yb-doped $\text{Sr}_2\text{Ce}_{0.95}\text{Yb}_{0.05}\text{O}_{3.975}$ sample under the condition with slightly lower $P_{\text{H}_2\text{O}} \sim 3.88 \times 10^{-4}$ atm [20]. While under wet atmosphere, the E_a in this work for the Er-doped $\text{Sr}_2\text{Ce}_{0.95}\text{Er}_{0.05}\text{O}_{3.975}$ sample at low temperature (≤ 500 °C) was ~ 0.93 eV with $P_{\text{H}_2\text{O}} \sim 0.03$ atm, which is higher than that (0.73 eV) of the reported Yb-doped $\text{Sr}_2\text{Ce}_{0.95}\text{Yb}_{0.05}\text{O}_{3.975}$ sample with $P_{\text{H}_2\text{O}} \sim 0.025$ atm at the same temperature region [20].

However, all samples, whether virgin or doped, experienced a sharp decline in conductivity when

the temperature exceeded 500 °C under wet atmosphere. The cause of this degradation will be further investigated and discussed later in this paper. **Figure 3b** shows a comparison for the complex part of conductivity plots of the virgin Sr_2CeO_4 sample recorded at 500 °C under dry and wet N_2 gas, revealing a noticeable increase in total conductivity under wet conditions. The significant enhancement in conductivity under wet atmosphere strongly suggests proton conduction in these materials, which is closely linked to the presence of oxygen vacancies in the material, as described by **Eq. (1)**. Confirmation of oxygen vacancies in the materials was obtained through both EPR and XPS, as shown in **Figures 3c, 3d** and **3e**, respectively. The EPR results indicated that the virgin Sr_2CeO_4 exhibited a symmetric signal ($g = 2.0081$) for oxygen vacancies, with broad signal possibly caused by wide distribution from disorder environment. A stronger signal was observed in Er-doped sample because of increased oxygen vacancies, Furthermore, the XPS results revealed a higher concentration of oxygen vacancies in the Er-doped sample compared to the virgin Sr_2CeO_4 , consistent with the EPR findings.

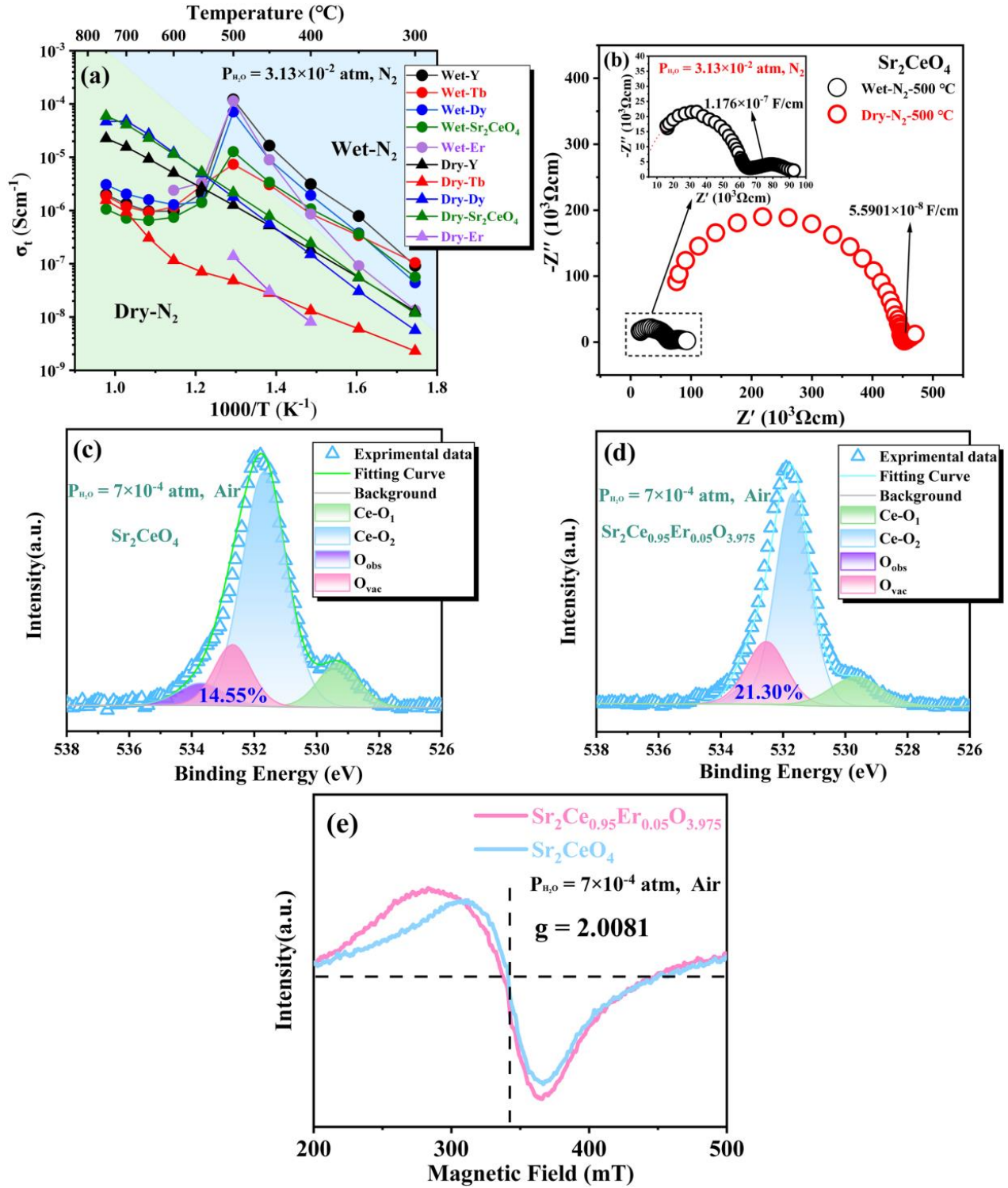


Figure 3. (a) The total conductivities as a function of temperature for $\text{Sr}_2\text{Ce}_{0.95}\text{M}_{0.05}\text{O}_{3.975}$ ($\text{M} = \text{Y, Dy, Er, Tb}$) under dry and wet N_2 gas; (b) The complex impedance plots of the virgin Sr_2CeO_4 material recorded under both dry and wet N_2 gas at 500°C ; (c, d) and (e) are XPS and EPR spectra of both the virgin and Er-doped Sr_2CeO_4 materials, respectively.

To confirm the interaction between water and oxygen vacancies, and to demonstrate the

successful inclusion of water into the crystal lattice, we conducted Raman spectroscopy and XRD diffraction analysis on both the dry and wet N₂ processed (placed in a sealed glass tube which was fed with the gas of $\sim 97\%N_2 + \sim 3\%H_2O$ accessed by bubbling the pure N₂ gas through room temperature deionized water for 12 h) samples. The peaks in the region of 50-100 cm⁻¹, as well as the peak around 150 cm⁻¹, appear notably wider, and the peak shifted towards higher values for the hydrated Sr₂CeO₄ sample (**Figure 4a**). These observations were consistent with phenomena observed in other typical proton conductors upon hydration [24]. **Figure 4b** shows the XRD patterns of the dry and hydrated Sr₂CeO₄ samples. The diffraction peaks of the hydrated sample collectively shifted to lower angles, indicating a larger cell volume compared to the dry sample, attributing to the incorporation of water into the structure.

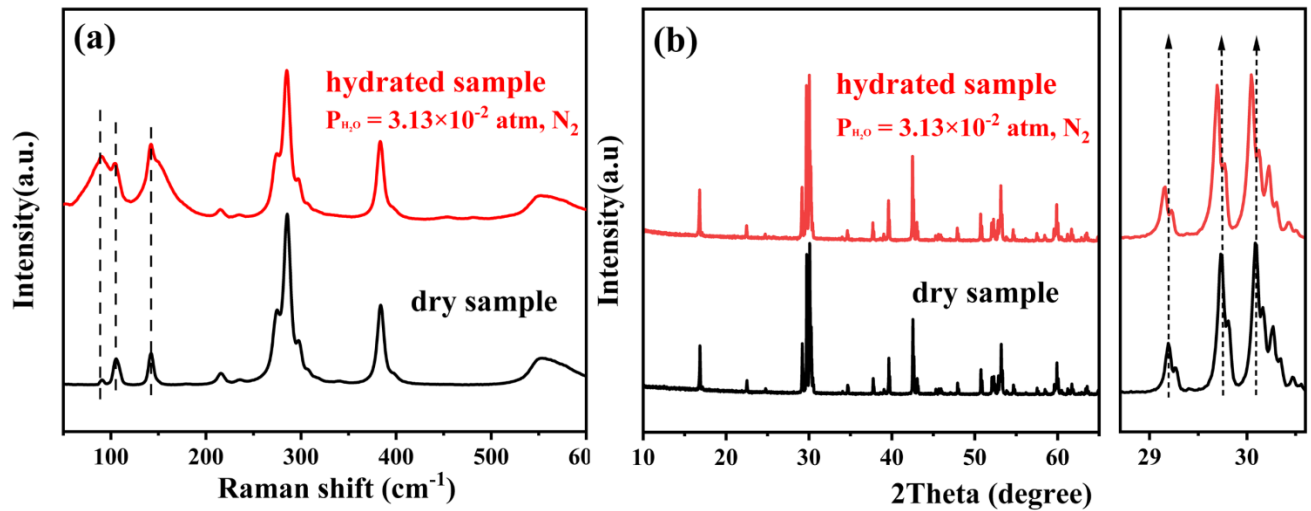


Figure 4. (a) Raman spectra of Sr₂CeO₄ samples with hydrated (b) XRD patterns of Sr₂CeO₄ samples with hydrated.

Although electrochemical impedance spectroscopy (EIS) is a simple and widely available method, the interpretation and attribution of the semicircles in the impedance spectra can become ambiguous as it depends upon user's expertise. The distribution of relaxation times (DRT) tool for

impedance analysis addresses this challenge. Through mathematical transformation, DRT results can be obtained from EIS measurements and used to analyze various relaxation processes in electrochemical systems. Each relaxation process corresponds to a specific relaxation time. By analyzing these relaxation times, we can resolve various electrochemical responses at the interface of the electrolyte and electrode with higher accuracy, such as ion migration, electron migration, grain and grain boundary response, and electrode response [22, 25-29]. Hence, DRT analysis was used to further investigate the detailed charge carrier transport process in Sr_2CeO_4 -based materials. **Figures 5a and 5b** show the AC impedance spectrum and corresponding fitting results, respectively based on the relaxation time of the D1 peak (7.73×10^{-7} s) and the capacitance value (1.72×10^{-10} F/cm), we can attribute it to grain and grain boundary transport [25]. **As shown in Figure 5c**, the two peaks at low frequency (D2 and D3) with relaxation time ranging from 10^{-4} to 1 s represent the electrode process at the electrode and interface: the D2 peak with a capacitance of $\sim 1.94 \times 10^{-7}$ F/cm corresponds to the charge transfer process, while the D3 peak with a capacitance of $\sim 4.79 \times 10^{-6}$ F/cm corresponds to the oxygen diffusion process [25].

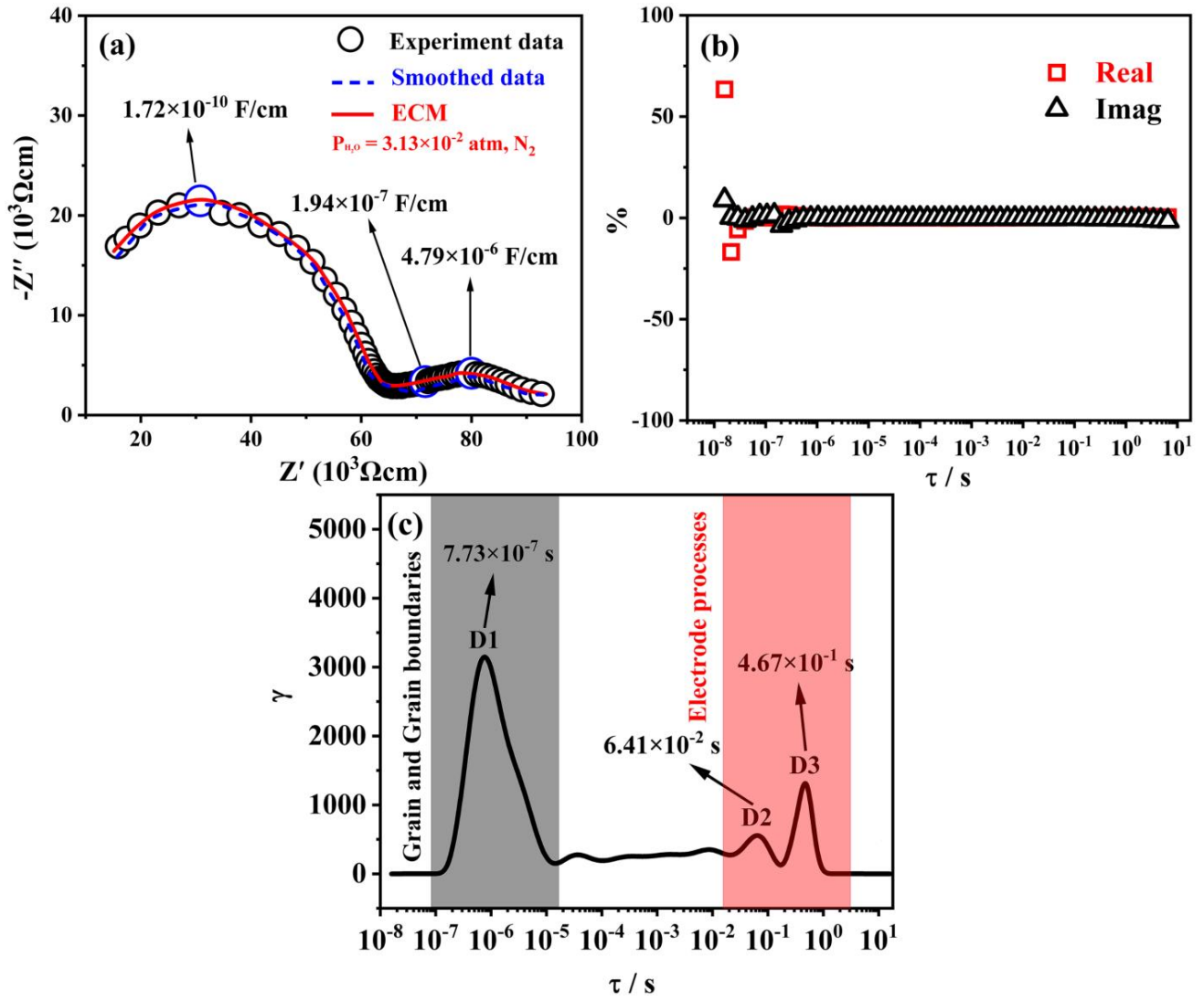


Figure 5. (a) The complex plots of the virgin Sr_2CeO_4 material recorded under wet N_2 gas at 500°C ; (b) Impedance spectrum fitting residual plot. (c) DRT analysis spectrum of Sr_2CeO_4 .

As aforementioned (**Figure 3a**), a sharp decrease in conductivity occurred for all samples under wet atmosphere and at temperature $> 500^\circ\text{C}$. Such behavior was not observed in previous work on Yb-doped Sr_2CeO_4 material [20], nor in samples measured here under dry atmosphere. In previous reported works, the samples were papered with the final sintering temperature of 1400°C which is apparently high than that in this work (1150°C), and therefore there is expected to be a big difference in the density between the samples in literature and in our work. Thus, to verify if it is the difference in density that leads to the huge deviation in electrical behaviors, we also prepared the

parent Sr_2CeO_4 material with a final sintering temperature of 1400 °C. The SEM analyses on the Sr_2CeO_4 materials prepared under 1150 °C and 1400 °C are demonstrated in **Figure 6a** and **6b**, respectively. We can see that there is obviously more pores in the sample sintered at 1150 °C than the sample sintered at 1400 °C. The relative density for these two samples, is 84.7% and 90.2%, respectively. However, the sample sintered at 1400°C with a higher density still experienced a sudden drop in conductivity at temperature above 500 °C, as shown in **Figure 6c** compared with that of the 1150 °C sintered sample measured on heating from 300 to 750 °C. The conductivity change trend was almost the same with that of the sample sintered at 1150 °C. In addition, we also measured these two samples on cooling from 750 to 300 °C under wet N_2 atmosphere, as shown in **Figure 6d**, which also disclosed a similar electrical behavior with that observed on heating. Such electrical behavior under wet condition observed in this work was indeed obviously different from that reported in literatures [20], and the heat history for the samples preparation and resultant density seems contributed little to the huge difference in electrical behaviors observed in our work and in literatures. The reason for such a great deviation between this work and previous reports remains unknown.

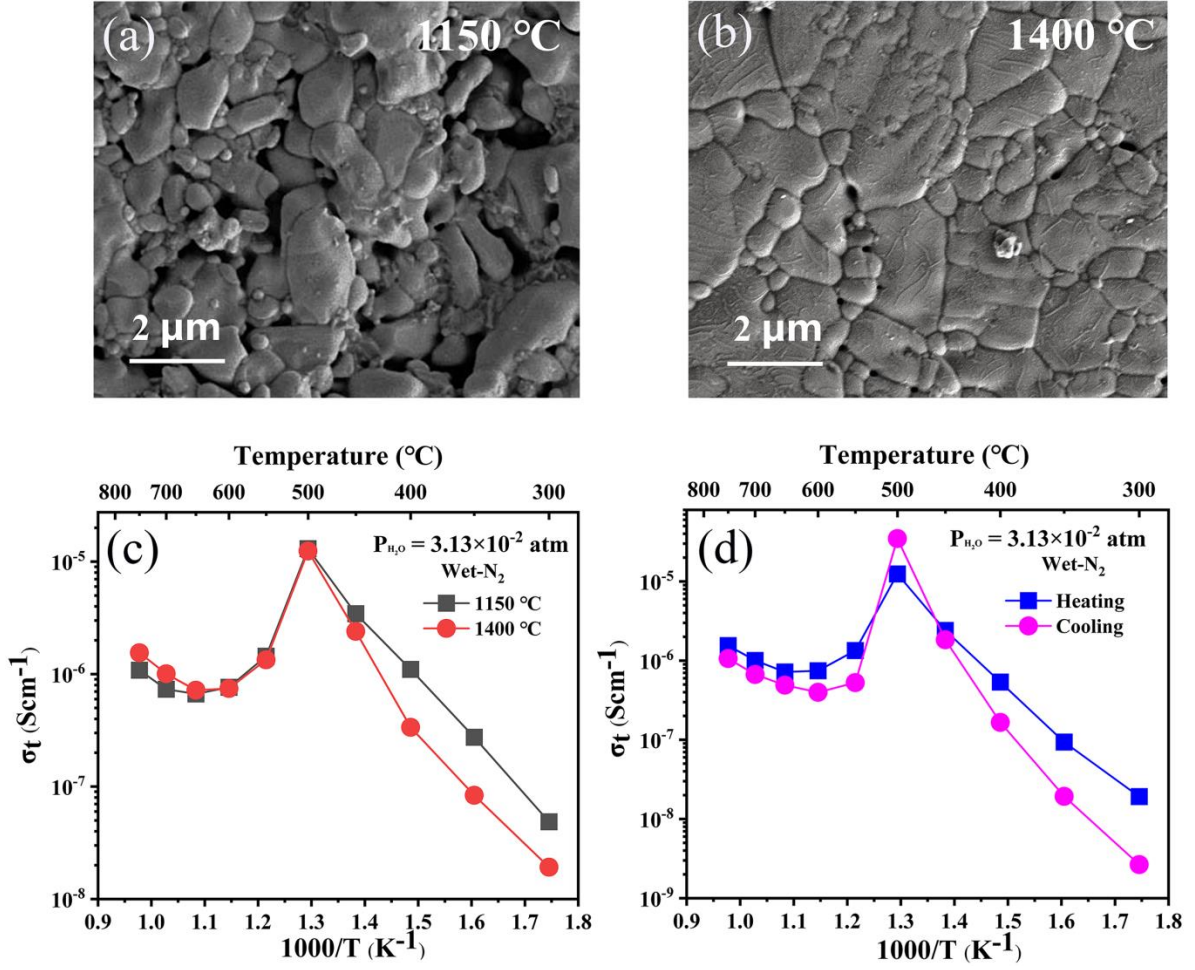


Figure 6. (a) and (b) are SEM figures for the Sr_2CeO_4 sample sintered at 1150 °C and 1450 °C; (c) and (d) are the Arrhenius plots for total conductivities of Sr_2CeO_4 samples.

Anyway, to explore the possible reason for the sharp decrease in conductivity occurred for all samples under wet atmosphere at temperature > 500 °C observed in this work, in-situ variable temperature XRD measurements were first carried out on the hydrated virgin Sr_2CeO_4 material to determine if there was a phase transition or decomposition at temperatures higher than 500 °C. As shown in **Figure 7a**, no apparent phase transition or decomposition was observed within the investigated temperature range. All peaks were attributed to the orthorhombic Sr_2CeO_4 phase and simply shifted toward lower 2θ as the temperature increased due to cell expansion. The refined cell parameters also linearly increase with temperature (**Figure 7b**). Additionally, due to the relatively

short holding time for in-situ XRD measurements at each temperature, slight decomposition that may lead to trace impurities below the detection limit of the XRD technique could not be excluded. Therefore, the hydrated and dry virgin Sr_2CeO_4 samples were annealed at 600 °C for different times, followed with ex-situ room temperature XRD measurements. Upon careful examination on the XRD patterns, as shown in **Figure 7c**, slight changes were observed at 2θ around 25.44°: for sample annealed at temperature below 500 °C (400 °C for 1 h here), only a peak that was difficult to detect was present. However, for hydrated samples annealed at temperature > 500 °C (600 °C here), the peak around 25° became more evident and wider compared to the ones annealed 400 °C which could be indexed to the $\text{SrO}_2 \cdot (\text{H}_2\text{O})_8$ phase (PDF#73-2219). Nevertheless, increasing the annealing time at 600 °C (3 h, 6 h, and 12 h) did not increase the intensity of this peak giving an indication of the structure's stability.

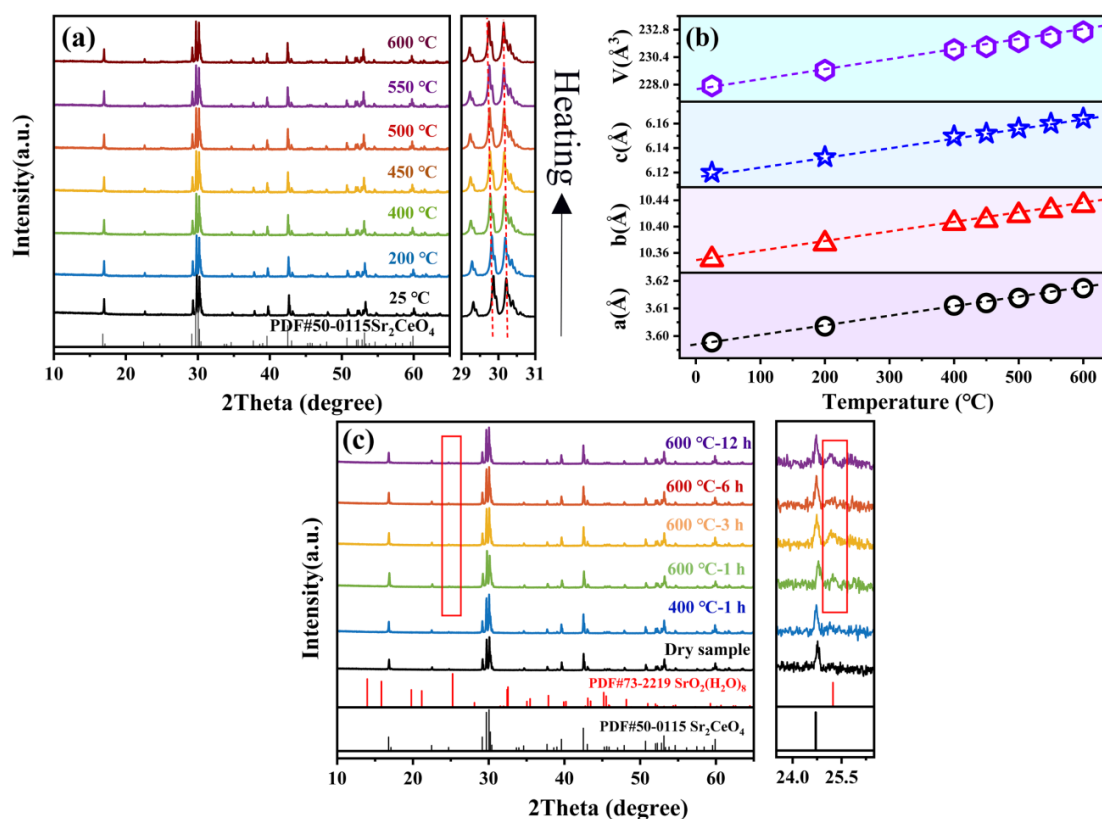


Figure 7. (a) Variable Temperature XRD pattern and (b) refined cell parameters of the hydrated

Sr₂CeO₄ samples under different temperatures; (c) XRD data of hydrated Sr₂CeO₄ materials at different holding times.

The Sr-segregation was further confirmed by the combined SEM/EDS analysis of both virgin and wet gas-annealed (550 °C) Sr₂CeO₄ samples. In the virgin sample, homogeneous distributions of all the elements appeared in both, surface and cross section (**Figure 8**). The atomic ratios of Sr/Ce on both surface and cross-section were similar (1.72 and 1.70, respectively) but lower than the nominal value of 2.0. This discrepancy may be due to the relatively lighter atomic weight of Sr compared to Ce, resulting in an underestimated value compared to Ce. However, in the hydrated and 550 °C annealed Sr₂CeO₄ sample, although the distributions of all elements, especially Sr, still displayed homogeneous distributions on both surface and cross-section, the atomic ratio of Sr/Ce on the surface was apparently higher than that in the cross-section, i.e. ~ 2.21 vs ~ 1.69. These results strongly support the conclusion of Sr-segregation in the hydrated samples upon annealing at temperature > 500 °C. These results remind us the commonly observed Sr-segregation in Sr-doped LaCo_{0.2}Fe_{0.8}O₃ and LaMnO₃ materials, as well as in classical proton conductors like BaCeO₃ and SrCeO₃[30-33], where Sr segregation on the surface greatly impacts electrical properties. In materials like LSCF or LSMO, it is exactly the electrostatic attraction of negatively charged A-site dopants near positively charged oxygen vacancies enriched at the surface that caused the Sr segregation on the surface or near the interface [34]. In our study, acceptor doping was designed on the Ce-sites rather than the Sr-sites, so the undoped Sr-sites are electrically neutral. Therefore the mechanism of Sr aggregation on the surface seems to be different from that in LSCF or LSMO. The formation of SrO₂•(H₂O)₈ layer between the electrode and electrolyte was supposed to occur happens through reaction with water. This layer causes a significant decrease in conductivity (**Figure 3**).

Furthermore, as increased annealing time at temperature $> 500\text{ }^{\circ}\text{C}$ under wet conditions did not lead to an increase in the amount of $\text{SrO}_2\cdot(\text{H}_2\text{O})_8$ phase (as can be seen from **Figure 7c**), it appears that the formation of such a layer acts as a barrier and prevents further inner reaction of Sr_2CeO_4 .

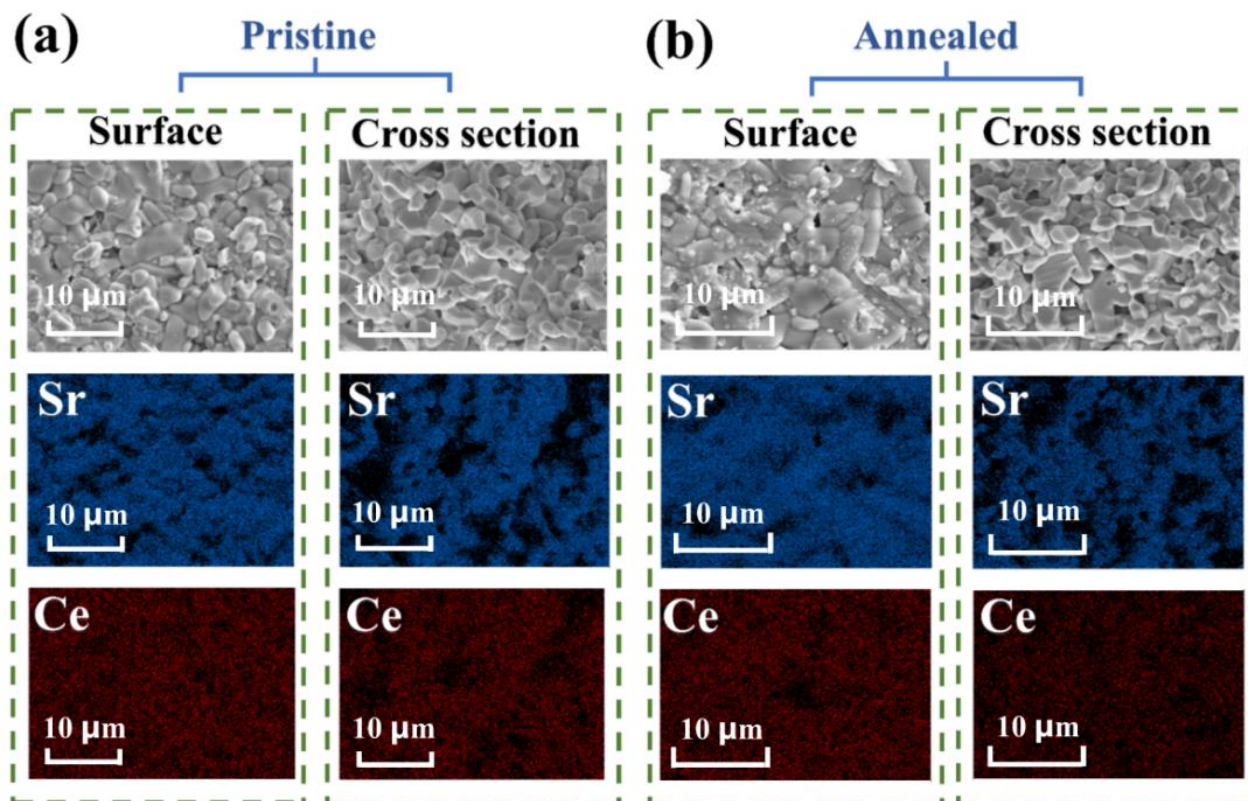


Figure 8. (a) Pristine Sr_2CeO_4 sample; (b) Annealed Sr_2CeO_4 samples in $550\text{ }^{\circ}\text{C}$ -Wet N_2 .

As mentioned earlier, the significant improvement conductivities under wet environment compared to dry conditions in both virgin and doped Sr_2CeO_4 materials strongly suggest proton conduction. However, to determine the exact charge carriers in these samples under wet environment, conductivities under different oxygen partial pressures ($p\text{O}_2$) were investigated and shown in **9b** for the selected Er-doped $\text{Sr}_2\text{Ce}_{0.95}\text{Er}_{0.05}\text{O}_{3.975}$ (named SCEO hereafter). As shown in **Figures 9a**, the strong spike in the low-frequency region ($< 10^2\text{ Hz}$) with an associated high capacitance ($> 10^{-7}\text{ F/cm}$) observed in the impedance plot recorded under wet N_2 , corresponds to the Warburg electrode response and diagnostic of ionic conduction [35], suggests a large electrode

polarization resistance due to the limited oxygen reduction reaction or hydrogen oxidation reaction on the symmetric Pt electrodes, as well as the large oxygen or hydrogen diffusion impedance. When the atmosphere changed to wet O₂ or wet H₂, such a spike collapsed to a small electrode response arc in the low-frequency range, which could be attributed to the significantly decreased impedance barrier for both the charge transfer ($\text{O}_2 + 4\text{e}^- = 2\text{O}^{2-}$, $\text{H}_2 - 2\text{e}^- = 2\text{H}^+$) and diffusion process with the increased oxygen or hydrogen partial pressure. Therefore, besides proton conduction, the oxygen conduction may also contribute to the total conductivities. Also, as demonstrated in **Figure 9b**, although there are no significantly enhancements in electrical conductivities at extremely low or high $p\text{O}_2$, compared to that at the middle $p\text{O}_2$ range, a slight slopes on the conductivity vs. $p\text{O}_2$ dependences at extremely low or high $p\text{O}_2$ region can still be seen, indicating that the *n*- (wet H₂) or *p*-type (wet O₂) electronic conduction may also contributed to the lower barrier at the sample/electrode interface, as observed in the impedance plots shown in **Figure 9b**. In fact, as shown in **Figure 9a** for the impedance plot recorded under wet N₂, the apparent Warburg electrode response may also partially arise from the blocking behavior of the strontium hydroxide layer. However, the greatly decreased electrode response resistance under wet H₂ and wet O₂ atmospheres suggested that the blocking behavior from the strontium hydroxide layer may be negligible, since the blocking behavior from the strontium hydroxide layer was expected to be independent on the measuring atmosphere. **Figure 9c** shows the conductivities of SCEO recorded under various water partial pressures ($P_{\text{H}_2\text{O}}$) within the temperature range of 300-500 °C. The conductivities increased with increasing $P_{\text{H}_2\text{O}}$ within the investigated temperature range. At a specific temperature of 500 °C (**Figure 9d**), the conductivities showed a relationship with $P_{\text{H}_2\text{O}}$ as $\sigma \sim p_{\text{H}_2\text{O}}^{1/2}$, which is in accordance with **Eq. (2)**, and can be derived from **Eq. (1)**, further supporting the proton conduction in SCEO.

$$[\text{OH}_\text{O}^\bullet] = (K[\text{O}_\text{O}^\times][\text{V}_\text{O}^{\bullet\bullet}])^{1/2} P_{\text{H}_2\text{O}}^{1/2} \quad (2)$$

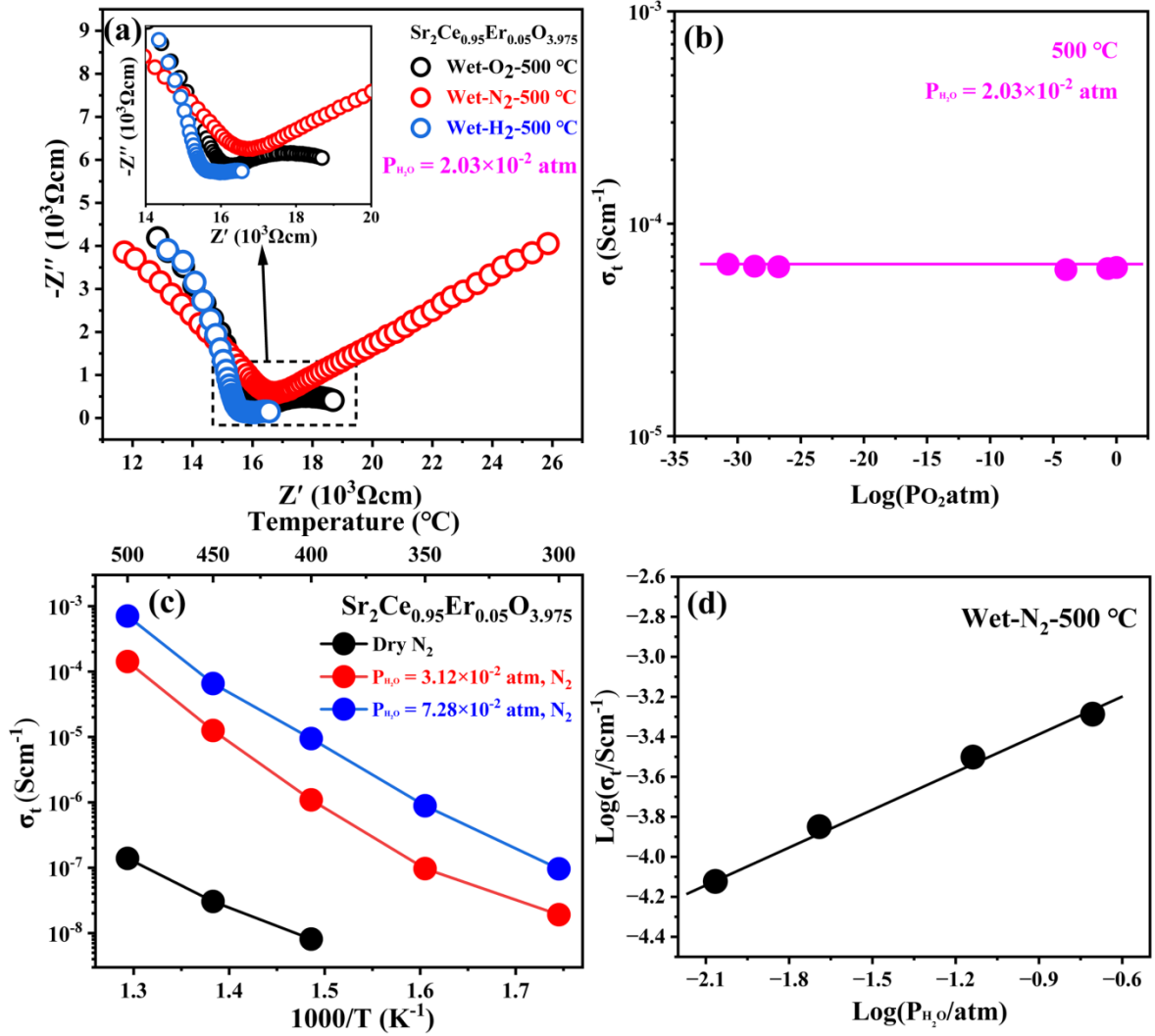


Figure 9. (a) AC impedance spectroscopy for the $\text{Sr}_2\text{Ce}_{0.95}\text{Er}_{0.05}\text{O}_{3.975}$ sample recorded at 500 °C in different atmosphere; (b) Total conductivity of $\text{Sr}_2\text{Ce}_{0.95}\text{Er}_{0.05}\text{O}_{3.975}$ samples as a function of $p\text{O}_2$ under constant temperature; (c) The Arrhenius plots for total conductivities of $\text{Sr}_2\text{Ce}_{0.95}\text{Er}_{0.05}\text{O}_{3.975}$ at different water vapor pressures; (d) Total conductivity of $\text{Sr}_2\text{Ce}_{0.95}\text{Er}_{0.05}\text{O}_{3.975}$ samples as a function of water vapor pressures under constant temperature.

To separate the contribution of oxygen ion and proton conduction in the hydrated SCEO, an electron and H^+ blocking method was used through a four-probe Hebb-Wagner cell, as can be appreciated from **Figure 10a**. Briefly, $\text{La}_{1.5}\text{Sr}_{0.5}\text{Ga}_3\text{O}_{7.25}$ (LSGO) is a pure oxygen ion conductor and was used as a blocking layer for electrons and protons. An additional porous Pt layer between SCEO

and LSGO, besides two reversible porous Pt electrodes, was applied to reduce the high SCEO/LSGO interface polarization resistance. The cell was placed in a quartz-glass tube furnace at 500 °C, under the flow of humid oxygen. The voltage drop of V_{mid} across the two wires that tie the middle section of the $\text{Sr}_2\text{Ce}_{0.95}\text{Er}_{0.05}\text{O}_{3.975}$ specimen was recorded, under a constant current flow of I , and then the oxide ionic conductivity (σ_o) could be calculated from the following equation.

$$\sigma_o = \frac{I \cdot d}{V_{\text{mid}} \cdot S} \quad (3)$$

where d denotes the separation distance between two probes for recording V , while S is the cross-sectional area of the sample. The constant current I was kept constant at various values in the range of 0.5–1.0 mA, as shown in **Figure 10b**. The results are provided in **Table 1** from which we can see that the oxygen ion conductivity (3.13×10^{-5} S/cm) contributed ~29% for the total ionic conduction of SCEO under a wet environment at 500 °C. This oxygen ion conductivity was two orders of magnitude higher than the total conductivity of SCEO under dry environment (only $\sim 3.13 \times 10^{-5}$ S/cm). Such a significant improvement in oxide ion conductivity under wet environment presents an interesting phenomenon and contradicts the decreased oxide ion conductivity that usually occurs in the typical proton conductors due to the decreased oxygen vacancy concentration upon hydration (according to **Eq. (1)**). Therefore, the greatly enhanced oxide ion conductivity in this work was supposed to thanks to the greatly reduced activation energy for **oxygen ion transport upon hydration**. **Since the conductivity is strongly related to the mobility and concentration of charge carries** and given the decreased concentration here for the oxygen vacancy when hydrated. The improved mobility of oxygen vacancy may be due to the expanded space for oxygen migration when hydrated, as proved from the XRD analysis results of the dry and wet sample, which thus led to reduced activation energy. Similar reductions in activation energy for oxide ion transport upon hydration have

been reported for acceptor-doped $\text{Ba}(\text{Zr}, \text{Ce})\text{O}_3$ material [36]. For instance, in Miruszewski et al.'s work on the hydrated $\text{BaCe}_{0.6}\text{Zr}_{0.2}\text{Y}_{0.2}\text{O}_3$ compound [37], they attributed the reduced activation energy of oxide ion transport to the trapping of protons by the negatively charged Y'_B defect, forming associated defect clusters of $(Y'_B - OH^\bullet_O)$. These clusters were unable to trap oxygen vacancy defects anymore, thereby increasing the mobility of remaining un-trapped oxygen vacancies. Additionally, Nyman et al.[38]. demonstrated that hydration of BaZrO_3 also reduces the activation energy for oxide ion transport through grain boundaries. Nyman et al. observed a decrease in oxide ion conductivity as the concentration of oxygen vacancies decreased upon hydration. However, in this paper, hydration led to a significant improvement in oxide ion conductivity. This discrepancy suggests that activation energy has a much greater influence than the concentration of oxygen vacancies on oxide ion conductivity in Sr_2CeO_4 -based material.

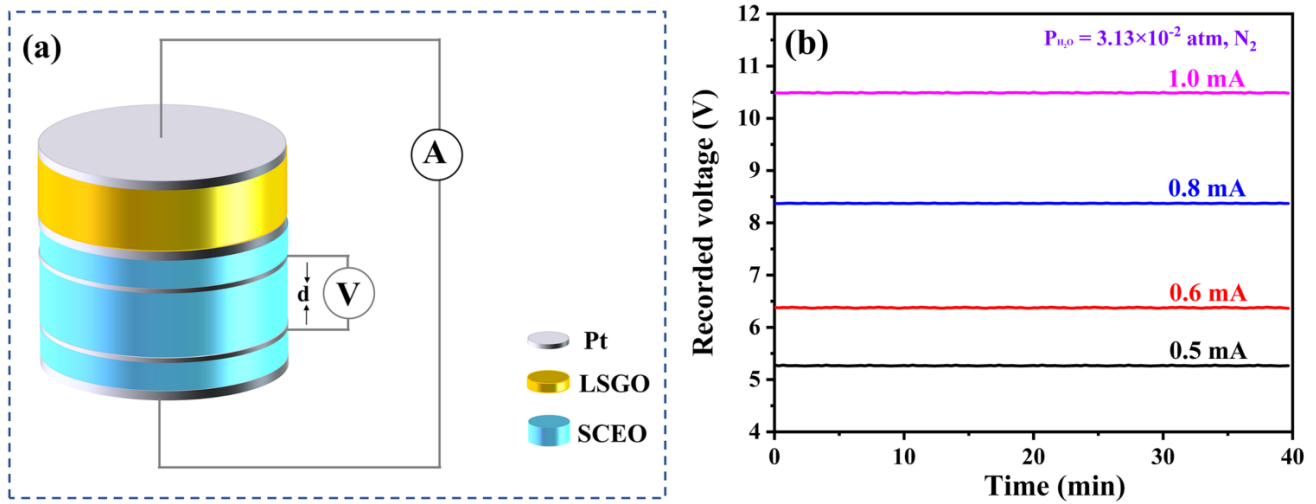


Figure 10 (a) The schematic of Four-probe Hebb–Wagner cell applied in this work; (b) recorded voltage under different currents

Table 1. The σ_o in $\text{Sr}_2\text{Ce}_{0.95}\text{Er}_{0.05}\text{O}_{3.975}$ derived from the four-probe Hebb-Waggoner cell method.

Current (I , mA)	Oxide ion conductivity (σ_o , S/cm)	Total conductivity (σ_t , S/cm)	Oxygen transport number (t_o)
0.5	3.126×10^{-5}	1.080×10^{-4}	0.2895
0.6	3.096×10^{-5}	1.080×10^{-4}	0.2867
0.8	3.142×10^{-5}	1.080×10^{-4}	0.2910
1.0	3.136×10^{-5}	1.080×10^{-4}	0.2904

Oxide ion and proton migration pathways. Subsequently, simulations were conducted using the bond-valence-based method to explore the migration paths for both oxide ions and protons in Sr_2CeO_4 . This method has been widely applied for investigating conduction pathways of Na^+ , H^+ , Li^+ and O^{2-} ions [39-44]. In this study, the crystal structure of Sr_2CeO_4 , as reported by Danieslon et al. [45], was used to calculate the bond-valence-based energy landscapes (BVELs) of both H^+ and O^{2-} . As shown in **Figures 11a-c**, the results revealed that ~ 0.603 eV of energy above the minimum energy (the most stable position for a tested proton), in one-dimensional (1D) pathways were formed between the tip oxygen and the equatorial oxygen of the CeO_6 octahedron along the c -axis $\langle 001 \rangle$ direction within the CeO_6 octahedron chains. To establish 2D or 3D pathways for proton migration (**Figures 11d-e**), ~ 0.84 eV was required in this paper which is relatively high for proton conduction. An activation energy of ~ 0.4 – 0.6 eV [25], can trigger the possibility of 3D migration for proton conduction in Sr_2CeO_4 , so this mechanism could not be fully ruled out. A typical 1D migration path of protons can be described as $\text{H}_{\text{O}1\text{a}}\text{---}s4\text{---}\text{H}_{\text{O}2\text{a}}\text{---}s2\text{---}s4\text{---}\text{H}_{\text{O}1\text{b}}\text{---}s4\text{---}\text{H}_{\text{O}2\text{b}}$ (where “ s ” denotes the saddle positions with the highest energy that a proton needs to overcome from one site to the next). The labels “a” and “b” are used to specify atoms with the same crystallographic coordinates in a unit

cell but different positions along the pathway. This pathway involves O2 and O1 sites, allowing the proton to hop from one of these two sites to another, assisted by the local saddle point sites s4 (0.736, 0.150, 0.188) and s2 (0.792, 0.1333, 0.5).

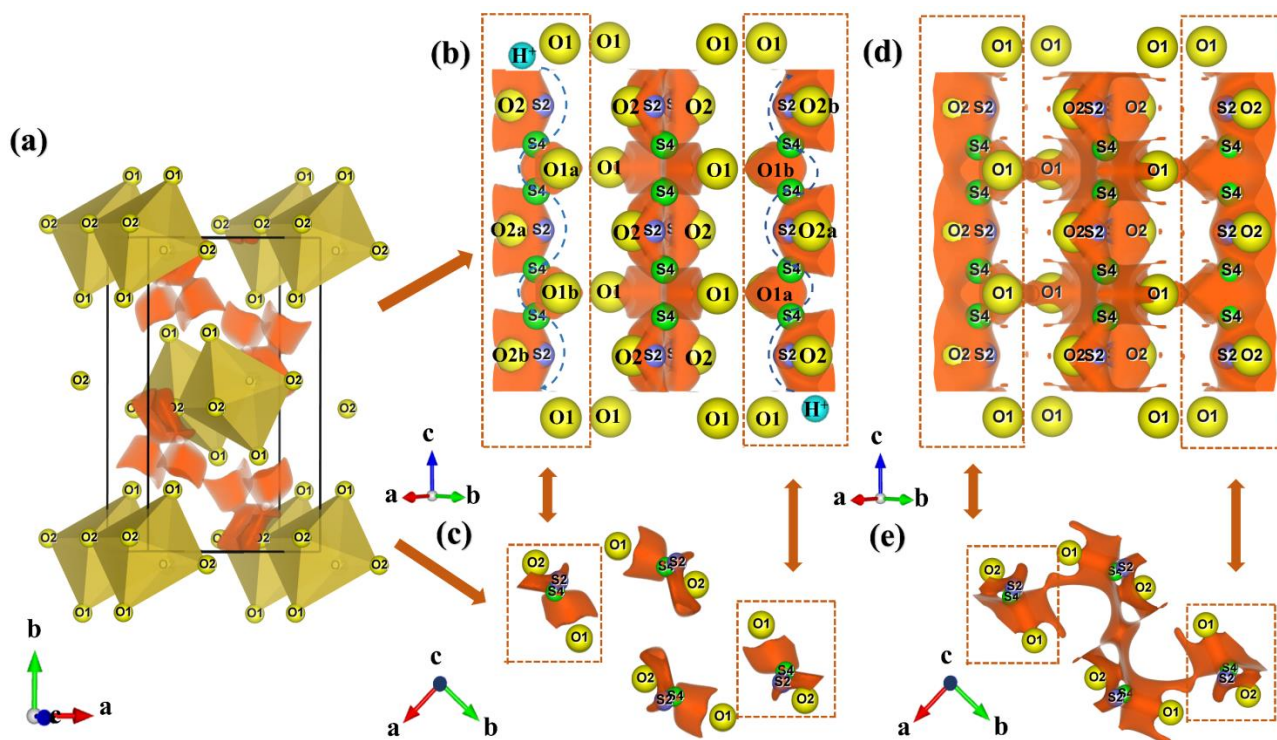


Figure 11. Picture (a), (b) and (c) show the BVLEs with energy iso-surfaces at 0.3 eV (1D), (d) and (e) are the BVLEs with energy iso-surfaces at 0.51 eV (2D-3D), respectively. The picture (b), (c), (d) and (e) are plotted in the range of $0.1 \leq x \leq 0.9$, $0.55 \leq y \leq 1.45$, $0.2 \leq z \leq 2.8$, the plotted range for pictures (a) is $0 \leq x \leq 1$, $0 \leq y \leq 1$, $0 \leq z \leq 3$, with all the Sr and Ce atoms omitted for clarity.

As shown in **Figures 12a-b**, for the one-dimensional path (1D), unlike protons, which diffuse between the top oxygen and the equatorial oxygen, the oxygen ion migration involves only the equatorial oxygen of the CeO_6 octahedral, with an activation energy of ~ 0.692 eV. The distance between two neighboring equatorial oxygens is ~ 3.53 Å. A typical path can be described as O2a—s5—i3—s5—O2b, where oxygen can hop from one equatorial position to another through the local interstitial site i3 (0.875, 0.508, 0) and saddle point s5 (0.194, 0.475, 0.25). A slight increase in

energy to ~ 0.700 eV yields other pathways along the $\langle 100 \rangle$ direction, forming 2D migration (**Figure 12c**), enabling equatorial oxygen to hop between neighboring CeO_6 octahedron chains. The shortest distance between two equatorial oxygens belonging to neighboring CeO_6 octahedrons chains is only 3.34 Å, even shorter than that between two equatorial oxygens within a CeO_6 octahedron along the c -direction. A typical pathway along the $\langle 100 \rangle$ direction can be described as $\text{O2a} \rightarrow \text{s6} \rightarrow \text{i2} \rightarrow \text{s6} \rightarrow \text{O2b} \rightarrow \text{s5} \rightarrow \text{i3} \rightarrow \text{s4} \rightarrow \text{i3} \rightarrow \text{s5} \rightarrow \text{O2a}$. The distance between the s5 site and the Ce atom is 2.29 Å, slightly higher than that of $\text{s6}-\text{Ce}$. However, as shown in **Figures 12d**, to realize the migration of oxygen ions along the $\langle 010 \rangle$ direction, forming 3D diffusion, a minimum activation energy of ~ 1.44 eV is required for the tip oxygen O1 atoms in one CeO_6 octahedron to hop to the nearest neighboring equatorial oxygen O2 in another octahedron chain. Again, although the activation energy of 1.44 eV for the 3D diffusion here is relatively high compared to that commonly observed in typical oxide ion conductors ($\sim 0.8\text{--}1.2$ eV) [46-48], we cannot fully rule out this possibility.

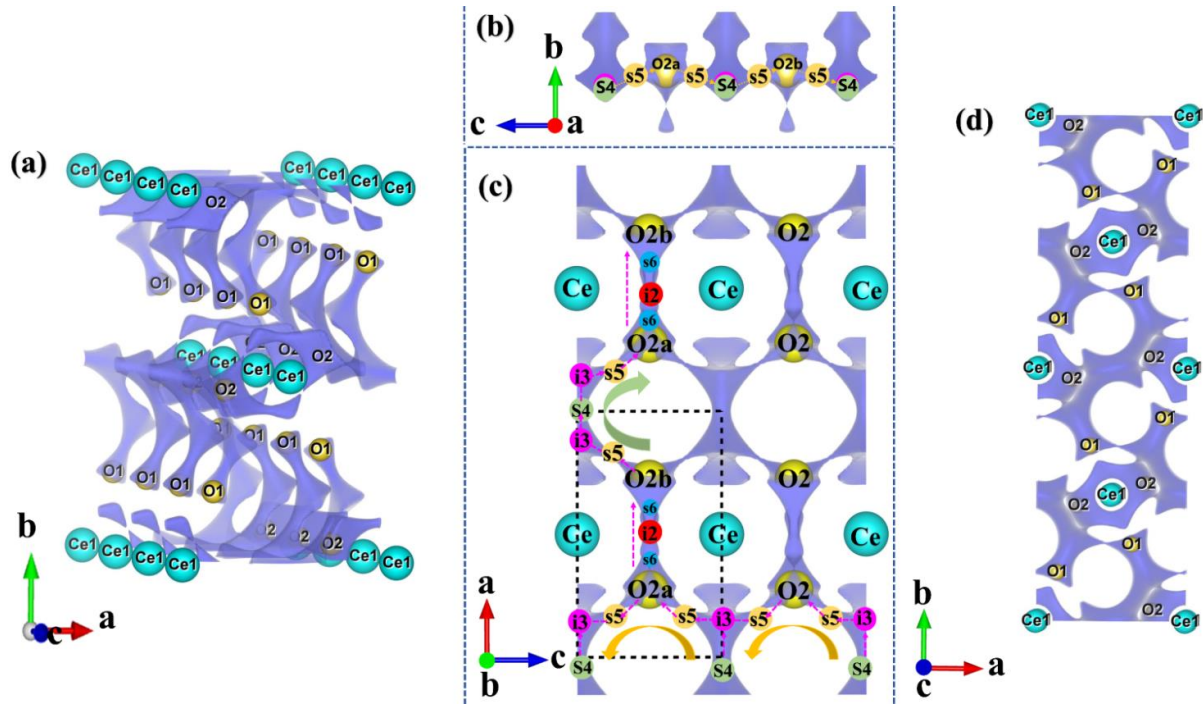


Figure 12. (a) Oxygen ion migration path 1D diagram of Sr_2CeO_4 material. The picture (a) are plotted in the range of $0 \leq x \leq 1$, $0 \leq y \leq 1$, $0 \leq z \leq 3$. the plotted range for pictures (b), (c), and (d)

are **(b)** $0.5 \leq x \leq 1$, $0.35 \leq y \leq 0.7$, $-0.2 \leq z \leq 2.2$, **(c)** $0.8 \leq x \leq 3$, $0.35 \leq y \leq 0.7$, $-0.2 \leq z \leq 2.2$, and **(d)** $0 \leq x \leq 1$, $0 \leq y \leq 2$, $0 \leq z \leq 1$, with all the Sr atoms omitted for clarity.

Conclusion.

In summary, four new rare earth-doped Sr_2CeO_4 materials were synthesized through the traditional solid state reaction method, with their electrical properties, phase stabilities, and conducting mechanisms were thoroughly studied. The results showed that all the virgin and doped Sr_2CeO_4 materials displayed obvious proton conduction under wet atmosphere, accompanied by enhanced oxide ion conduction within a wide range of oxygen partial pressures at temperatures $\leq 500^\circ\text{C}$. The ionic conductivity at 500°C under wet conditions for Er-doped Sr_2CeO_4 was $1.08 \times 10^{-4} \text{ S/cm}$, which is nearly three orders of magnitude higher than that reported values for best performing Yb-doped Sr_2CeO_4 material. However, at temperatures $> 500^\circ\text{C}$ in a humid environment, the reaction of the Sr_2CeO_4 -based materials with water led to the formation of a $\text{SrO}_2 \cdot (\text{H}_2\text{O})_8$ layer on the surface of the ceramic pellets, and caused a significant decrease in conductivity, although this layer could prevent further reaction of water with the inner part of these Sr_2CeO_4 -based materials. The proton and oxide ion migration mechanisms in Sr_2CeO_4 -based materials were studied for the first time and preferred a 1D and 2D pathway, respectively, strongly related to the CeO_6 tetrahedral chains.

Conflicts of interest

There are no conflicts of interest to declare.

Acknowledgements

This work was supported by the Guangxi Natural Science Foundation (No. 2021GXNSFFA220002), the Science and Technology Plan of Guangxi (Nos. AA21238001 and ZY22096019), National Natural Science Foundation of China (No.21965008), the Key Research and Development Program of Shandong Province.

Appendix A. Supplementary data

Reference

- [1] N. P. Brandon, Z. Kurban, Clean energy and the hydrogen economy, *Philos Trans A Math Phys Eng Sci.* 375 (2017) 20160400.
- [2] P. H. Cyril, G. Saravanan, Development of advanced materials for cleaner energy generation through fuel cells, *New J. Chem.* 44 (2020) 19977-19995.
- [3] S. A. Rasaki, C. Liu, C. Lao, H. Zhang, Z. Chen, The innovative contribution of additive manufacturing towards revolutionizing fuel cell fabrication for clean energy generation: A comprehensive review, *Renew. Sust. Energ. Rev.* 148 (2021) 111369.
- [4] L. S. Benneer, Energy Justice, Decarbonization, and the Clean Energy Transformation, *Annu. Rev. Resour. Economics.* 14 (2022) 647-668.
- [5] P. Gupta, B. Toksha, M. Rahaman, A Critical Review on Hydrogen Based Fuel Cell Technology and Applications, *Chem Rec.* 24 (2024) 202300295.
- [6] Y. Yuan, H. Yu, A. Podpirka, P. Ostdiek, R. Srinivasan, S. Ramanathan, Negative Differential Resistance in Oxygen-ion Conductor Yttria-stabilized Zirconia for Extreme Environment Electronics, *ACS Appl. Mater.* 14 (2022) 40116-40125.
- [7] M.-S. Park, K. Jo, H. Lee, H. Lee, $\text{Lu}_2\text{O}_3\text{-Y}_2\text{O}_3\text{-ZrO}_2$: A Lu^{3+} co-doped YSZ system—Oxygen-ion conductor with high electrical conductivity and improved mechanical properties, *J. Mater. Res. Technol.* 27 (2023) 8403-8411.
- [8] Y. Zhang-Steenwinkel, Q. Yu, F. P. F. Van Berkel, M. M. A. Van Tuel, B. Rietveld, H. Tu, High performance solid-oxide fuel cell: Opening windows to low temperature application, *Int. J. Hydrogen Energy.* 41 (2016) 5824-5832.
- [9] B. C. Yang, J. Koo, J. W. Shin, D. Go, J. H. Shim, J. An, Direct Alcohol-Fueled Low-Temperature Solid Oxide Fuel Cells: A Review, *Energy Technol.* 7 (2018) 5-19.
- [10] H. Su, Y. H. Hu, Progress in low-temperature solid oxide fuel cells with hydrocarbon fuels, *Chem. Eng. J. (Lausanne).* 402 (2020) 126235.
- [11] G. Yang, C. Su, H. Shi, Y. Zhu, Y. Song, W. Zhou, Z. Shao, Toward Reducing the Operation Temperature of Solid Oxide Fuel Cells: Our Past 15 Years of Efforts in Cathode Development, *Energy Fuels.* 34 (2020) 15169-15194.
- [12] M. Fallah Vostakola, B. Amini Horri, Progress in Material Development for Low-

Temperature Solid Oxide Fuel Cells: A Review, *Energies*. 14 (2021) 1280.

- [13] J. Yang, Y. Lv, X. Xu, X. Song, H. Wei, M. Tian, J. Xu, Remarkably high proton conductivity in cubic perovskite-related Ba_3WO_6 , *J. Mater. Chem. A*. 10 (2022) 16697-16703.
- [14] S. G. a. a. V. Virkar, Thermodynamic Stabilities of SrCeO_3 and BaCeO_3 Using a Molten Salt Method and Galvanic Cells, *J. Electrochem. Soc.* 140 (1993) 1060-1065.
- [15] W. Zając, D. Rusinek, K. Zheng, J. Molenda, Applicability of Gd-doped BaZrO_3 , SrZrO_3 , BaCeO_3 and SrCeO_3 proton conducting perovskites as electrolytes for solid oxide fuel cells, *Open Chem.* 11 (2013) 471-484.
- [16] D. Vignesh, B. K. Sonu, E. Rout, Factors Constituting Proton Trapping in BaCeO_3 and BaZrO_3 Perovskite Proton Conductors in Fuel Cell Technology: A Review, *Energy Fuels*. 36 (2022) 7219-7244.
- [17] R. Kannan, K. Singh, S. Gill, T. Fürstenhaupt, V. Thangadurai, Chemically Stable Proton Conducting Doped BaCeO_3 -No More Fear to SOFC Wastes, *Sci. Rep.* 3 (2013) 2138.
- [18] M. Stefanski, L. Marciniak, D. Hreniak, W. Strek, Influence of grain size on optical properties of Sr_2CeO_4 nanocrystals, *J Chem Phys.* 142 (2015) 184701.
- [19] A. N. Shirsat, K. N. G. Kaimal, S. R. Bharadwaj, D. Das, Thermodynamic stability of Sr_2CeO_4 , *Thermochim. Acta.* 447 (2006) 101-105.
- [20] V. P. Gorelov, V. B. Balakireva, V. A. Vorotnikov, Proton Conductivity of Acceptor-Doped Sr_2CeO_4 , *Inorg. Mater.* 55 (2019) 1167-1171.
- [21] A. A. Coelho, TOPAS-academic, Coelho Software, Brisbane, Australia. (2007).
- [22] H. Li, Z. Lyu, M. Han, Robust and fast estimation of equivalent circuit model from noisy electrochemical impedance spectra, *Electrochim. Acta.* 422 (2022) 140474.
- [23] D. Yadav, U. Kumar, S. Upadhyay, Study of structural, electrical, and photoluminescent properties of SrCeO_3 and Sr_2CeO_4 , *Journal of Advanced Ceramics*. 8 (2019) 377-388.
- [24] A. Slodczyk, P. Colomban, D. Lamago, M.-H. Limage, F. Romain, S. Willemin, B. Sala, Phase transitions in the H^+ -conducting perovskite ceramics by the quasi-elastic neutron and high-pressure Raman scattering, *Ionics*. 14 (2007) 215-222.
- [25] S. Yu, Z. Wang, L. Yang, J. Liu, R. Guan, Y. Xiao, T. He, Enhancing the sinterability and electrical properties of $\text{BaZr}_{0.1}\text{Ce}_{0.7}\text{Y}_{0.2}\text{O}_{3-\delta}$ proton-conducting ceramic electrolyte, *J. Am.*

Ceram. Soc. 104 (2020) 329-342.

- [26] M. Saccoccio, T. H. Wan, C. Chen, F. Ciucci, Optimal Regularization in Distribution of Relaxation Times applied to Electrochemical Impedance Spectroscopy: Ridge and Lasso Regression Methods - A Theoretical and Experimental Study, *Electrochim. Acta.* 147 (2014) 470-482.
- [27] B. A. Boukamp, A. Rolle, Analysis and Application of Distribution of Relaxation Times in Solid State Ionics, *Solid State Ion.* 302 (2017) 12-18.
- [28] B. A. Boukamp, A. Rolle, Use of a distribution function of relaxation times (DFRT) in impedance analysis of SOFC electrodes, *Solid State Ion.* 314 (2018) 103-111.
- [29] J. Hong, A. Bhardwaj, H. Bae, I.-H. Kim, S.-J. Song, Electrochemical Impedance Analysis of SOFC with Transmission Line Model Using Distribution of Relaxation Times (DRT), *J. Electrochem. Soc.* 167 (2020) 114504.
- [30] Z. M. D. A. S. P. Simner, M. H. Engelhard, and J. W. Stevenson*, Degradation Mechanisms of La – Sr – Co – Fe – O₃ SOFC Cathodes, *Electrochem. Solid-State Lett.* 9 (2006) A478-A481.
- [31] W. Lee, J. W. Han, Y. Chen, Z. Cai, B. Yildiz, Cation size mismatch and charge interactions drive dopant segregation at the surfaces of manganite perovskites, *J Am Chem Soc.* 135 (2013) 7909-7925.
- [32] S. M. H. Kwang Hyun Ryu, Chemical stability and proton conductivity of doped BaCeO₃ – BaZrO₃ solid solutions, *Solid State Ion.* 125 (1999) 355-367.
- [33] W. Wang, D. Medvedev, Z. Shao, Gas Humidification Impact on the Properties and Performance of Perovskite-Type Functional Materials in Proton-Conducting Solid Oxide Cells, *Adv. Funct. Mater.* 28 (2018) 1802592.
- [34] Y. Chen, Y. Chen, D. Ding, Y. Ding, Y. Choi, L. Zhang, S. Yoo, D. Chen, B. Deglee, H. Xu, Q. Lu, B. Zhao, G. Vardar, J. Wang, H. Bluhm, E. J. Crumlin, C. Yang, J. Liu, B. Yildiz, M. Liu, A robust and active hybrid catalyst for facile oxygen reduction in solid oxide fuel cells, *Energy & Environmental Science.* 10 (2017) 964-971.
- [35] D. C. S. By John T. S. Irvine, * and Anthony R. West *, *Electroceramics : Characterization by Impedance Spectroscopy*, *Adv. Mater. (Weinheim, Ger.).* 2 (1990) 132-138.

- [36] I. Oikawa, H. Takamura, Correlation among Oxygen Vacancies, Protonic Defects, and the Acceptor Dopant in Sc-Doped BaZrO₃ Studied by ⁴⁵Sc Nuclear Magnetic Resonance, *Chem. Mater.* 27 (2015) 6660-6667.
- [37] T. Miruszewski, K. Dzierzgowski, P. Winiarz, S. Wachowski, A. Mielewczyk-Gryn, M. Gazda, Hebb–Wagner polarization method for determining the oxygen ion conductivity in barium cerate-zirconate, *J. Mater. Chem. A*. 10 (2022) 7218-7227.
- [38] B. Joakim Nyman, E. E. Helgee, G. Wahnström, Oxygen vacancy segregation and space-charge effects in grain boundaries of dry and hydrated BaZrO₃, *Appl. Phys. Lett.* 100 (2012) 061903.
- [39] M. Avdeev, M. Sale, S. Adams, R. P. Rao, Screening of the alkali-metal ion containing materials from the Inorganic Crystal Structure Database (ICSD) for high ionic conductivity pathways using the bond valence method, *Solid State Ion.* 225 (2012) 43-46.
- [40] M. Duchardt, S. Neuberger, U. Ruschewitz, T. Krauskopf, W. G. Zeier, J. Schmedt Auf Der Günne, S. Adams, B. Roling, S. Dehnen, Superior Conductor Na_{11.1}Sn_{2.1}P_{0.9}Se₁₂: Lowering the Activation Barrier of Na⁺ Conduction in Quaternary 1–4–5–6 Electrolytes, *Chem. Mater.* 30 (2018) 4134-4139.
- [41] R. Inoue, K. Fujii, M. Shiraiwa, E. Niwa, M. Yashima, A new structure family of oxide-ion conductors Ca_{0.8}Y_{2.4}Sn_{0.8}O₆ discovered by a combined technique of the bond-valence method and experiments, *Dalton Trans.* 47 (2018) 7515-7521.
- [42] Y. Yasui, E. Niwa, M. Matsui, K. Fujii, M. Yashima, Discovery of a Rare-Earth-Free Oxide-Ion Conductor Ca₃Ga₄O₉ by Screening through Bond Valence-Based Energy Calculations, Synthesis, and Characterization of Structural and Transport Properties, *Inorg Chem.* 58 (2019) 9460-9468.
- [43] Y. Sallemi, R. Marzouki, Y. Ben Smida, A. A. El-Zahhar, M. Graia, Synthesis, characterization, electrical properties, and Na⁺ transport pathways simulation in Na₂ZnP_{1.5}As_{0.5}O₇, *Ionics*. 27 (2021) 3051-3061.
- [44] Y. Guo, W. Guo, L. Lei, J. Xu, Oxide ion conduction and transporting mechanism in the layered perovskite-related material Sr₂Nb₂O₇, *Scr. Mater.* 221 (2022) 114962.
- [45] E. Danielson, M. Devenney, D. M. Giaquinta, J. H. Golden, R. C. Haushalter, E. W.

- Mcfarland, D. M. Poojary, C. M. Reaves, W. H. Weinberg, X. D. Wu, A rare-earth phosphor containing one-dimensional chains identified through combinatorial methods, *Science*. 279 (1998) 837-839.
- [46] A. Platonenko, D. Gryaznov, Y. F. Zhukovskii, E. A. Kotomin, Ab initio simulations on charged interstitial oxygen migration in corundum, *Nucl. Instrum. Methods Phys. Res., Sect. B*. 435 (2018) 74-78.
- [47] T. T. Mayeshiba, D. D. Morgan, Factors controlling oxygen migration barriers in perovskites, *Solid State Ion*. 296 (2016) 71-77.
- [48] J. Hanzig, M. Zschornak, E. Mehner, F. Hanzig, W. Münchgesang, T. Leisegang, H. Stöcker, D. C. Meyer, The anisotropy of oxygen vacancy migration in SrTiO_3 , *J. Phys.: Condens. Matter*. 28 (2016) 225001.